

A homogenized strain model for Ni-Mn-Ga driven with collinear field and stress

LeAnn E. Faidley, Marcelo J. Dapino, Gregory N. Washington,

The Ohio State University, 650 Ackerman Road, Suite 255, Columbus, OH, USA, 43202

ABSTRACT

Ferromagnetic Shape Memory Alloys (FSMAs) in the nickel manganese gallium system have been shown to exhibit large magnetically induced strains of up to 9.5% due to magnetically driven twin variant reorientation. In order for this strain to be reversible, however, an external restoring stress or magnetic field needs to be applied orthogonal to the field and hence the implementation of Ni-Mn-Ga in applications involves the use of electromagnets, which tend to be heavy, bulky and narrowband. In previous work at The Ohio State University a sample of $\text{Ni}_{50}\text{Mn}_{28.7}\text{Ga}_{21.3}$ has been shown to exhibit reversible compressive strains of -4200 microstrain along its [001] direction when a magnetic field is applied along this same direction and no externally applied restoring force is present. This reversible strain is possible because of an internal stress field associated with pinning sites induced during manufacture of the crystal. This paper analyzes the switching between two variant orientations in the presence of magnetic fields (Zeeman energy) and pinning sites (pinning energy) through the formulation of a Gibbs energy functional for the crystal lattice. Minimization of the Gibbs free energy yields a strain kernel which represents the predicted behavior of an idealized 2-dimensional homogeneous single crystal with a single twin boundary and pinning site. While adequate, the kernel has limitations because it does not account for the following: (a) Ni-Mn-Ga consists of a large number of twin variants and boundaries, (b) the strength of the pinning sites may vary, and (c) the local and applied magnetic field will differ due to neighbor-to-neighbor interactions. These limiting factors are addressed in this paper by considering stochastic homogenization. Stochastic distributions are used on the interaction field and on the pinning site strength, yielding a phenomenological model for the bulk strain behavior of $\text{Ni}_{50}\text{Mn}_{28.7}\text{Ga}_{21.3}$. The model quantifies both the hysteresis and saturation of the strain. Constrained optimization is used to determine the necessary parameters and an error analysis is performed to assess the accuracy of the model for various loading conditions.

Keywords: Ferromagnetic Shape Memory Alloys, Homogenized model, Collinear Field-Stress, Solenoid actuator

1. INTRODUCTION

Large magnetic field-induced strains as large as 9.5% have been observed in nickel manganese gallium (Ni-Mn-Ga) martensites exposed to magnetic fields of 400 kA/m.¹⁻³ Due to the field activation, the frequency response of Ni-Mn-Ga alloys can be higher than that exhibited through thermal activation in shape memory alloys.⁴ These properties are significant for actuator and sensor applications in which large deformations and broad frequency bandwidths are required.

As is the case with shape memory materials, the large deformations exhibited by Ni-Mn-Ga alloys originate in the pseudoelasticity associated with the reorientation of martensitic twin variants under the action of magnetic fields. Unlike nickel titanium and other shape memory materials, in which the ability to do work stems from thermomechanical transformation between the martensite and austenite phases, the main actuation mechanism in Ni-Mn-Ga is the twin variant reorientation which takes place in the low temperature martensite phase and is driven by magnetic fields or mechanical stresses. Since in Ni-Mn-Ga magnetic fields and compressive stresses applied collinearly favor the same variant, an external force must be applied orthogonal to the applied field

Further author information: (Send correspondence to M.J.D.)

L.E.F.: E-mail: faidley.1@osu.edu, Telephone: 1-614-292-8685

M.J.D.: E-mail: dapino.1@osu.edu, Telephone: 1-614-688-3689

G.N.W.: E-mail: washington.88@osu.edu, Telephone: 1-614-292-8486

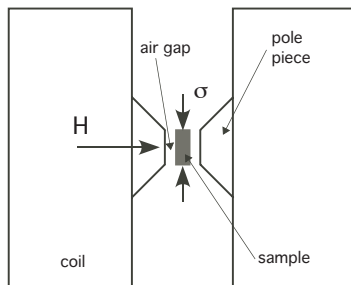


Figure 1. Diagram of field and stress orientations in an electromagnet.

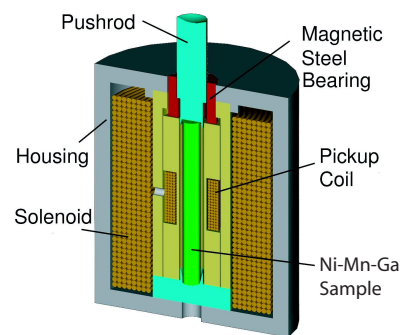


Figure 2. Solenoid Ni-Mn-Ga transducer for use in dynamic actuator and sensor applications.

to restore the twin variants and thus obtain bidirectional deformations. In applications, this is often done by placing a rectangular sample in an electromagnet with the magnetic field applied along the $[110]$ crystallographic direction of the parent phase and a bias compressive stress applied along the $[001]$ direction.⁵ This configuration is shown in Figure 1.

In a previous study, Malla et al.⁶ have established that large reversible strains of -0.41% are possible in $\text{Ni}_{50}\text{Mn}_{28.7}\text{Ga}_{21.3}$ exposed to alternating magnetic fields along the $[001]$ direction of the parent austenite phase with *no external restoring force*.^{6,7} This unexpected result suggests the presence of pinning sites or point defects in the alloy which act as localized energy potentials that oppose twin boundary motion and provide an otherwise nonexistent restoring force when the magnetic field is removed. The presence of pinning sites also explains the reduced deformations relative to alloys capable of over 6% strain, in which twin boundary motion is largely unimpeded. Richard et al.⁸ have shown that Ni-Mn-Ga alloys are extremely susceptible to impurities. Large, incoherent sulfide and tantalum inclusions have been observed as well as titanium precipitates. It was concluded that for the large, high energy inclusions observed, dislocations would have to loop around the impurities in order for twin boundary motion to occur. Since the observed Ti precipitates are much smaller, it was argued that the mechanism of dislocation motion in the presence of Ti precipitates is most likely cutting through the particles, as opposed to looping. By cutting, the twin boundaries form two new interfaces which provide a low-energy path for dislocation movement as compared to looping around the particles. It was estimated that the small Ti-rich precipitates have a strength of approximately $0.53 K_u$, thus acting as pinning sites which could be overcome by the application of sufficiently large magnetic fields. These small precipitates do not seem to impact the magnetic field induced strain (MFIS) of the alloys studied as strains of 6% were observed.

This paper is focused on the development and implementation of a homogenized thermodynamic model for twin boundary reorientation in the presence of pinning sites. As established by Malla et al.,⁶ low-energy pinning sites do not contribute to the mechanism for reversible MFIS in the alloy investigated; during the first few field cycles after manufacture of the alloy, the twin boundaries have passed through these sites and permanently attached themselves to the higher-energy sites. Hence, the model is constructed on the assumption that twin boundaries are normally pinned to point defects whose energy is greater than the anisotropy energy. The model provides an additional component to the current description of the strain mechanism in Ni-Mn-Ga and lays the groundwork for future work on implementation and control of solenoid Ni-Mn-Ga transducers like that shown in Figure 2. Because solenoid transducers can be designed around a closed magnetic circuit, they can potentially offer higher efficiency and enhanced frequency bandwidth relative to their electromagnet counterparts. These enhanced properties can possibly offset the reduced deformations produced by the Ni-Mn-Ga element in this configuration.

2. STRAIN MECHANISMS

The strain mechanism for Ni-Mn-Ga is well established.⁹⁻¹¹ As Ni-Mn-Ga cools from the high temperature austenite phase to the low temperature martensite phase, a self-accommodating twinned structure results due to the minimization of the strain energy generated from the mismatch between the cubic and tetragonal lattices. A simplified two-dimensional representation of this twinned structure is shown in Figure 3. At zero field the material consists of two perpendicular variants which are separated by a twin boundary as illustrated in panel (a). Each variant consists of several distinct magnetic domains which are divided by 180° walls. The magnetic domain volume fraction is denoted a . At small fields H , all of the magnetization vectors remain aligned with the magnetically easy, short c -axis of each variant and the magnetic domains disappear as shown in panel (b). Since we are interested in the behaviors at medium to large fields, $a = 1$ is assumed.

Let us consider the case, as in $\text{Ni}_{50}\text{Mn}_{28.7}\text{Ga}_{21.3}$, in which the twin boundaries are pinned to inclusions - modeled as springs and represented by black dots in Figure 3 - which have energies larger in magnitude than the anisotropy energy of the sample. Alloys in the Ni-Mn-Ga system have large magnetic anisotropy energies compared to the energy necessary to reorient the unit cells at the twin boundary. Thus, as the magnetization vectors attempt to align with the applied magnetic field, the unit cells along the twin boundary will switch orientation such that their c -axis is more closely aligned with the field. This results in the growth of favorable variants at the expense of unfavorable ones through twin boundary motion and the overall axial contraction of the bulk sample, as depicted in panel (c). The field does not provide enough energy to overcome the energy barrier provided by the pinning sites, however. Instead, the twin boundaries loop around the pinning sites and as they do work against the pinning energy, energy is dissipated. Saturation is achieved when the field energy is large enough to overcome the anisotropy energy and the magnetic moments align with the field without changing the orientation of the crystal, as shown in panel (d). When the field is removed (panel (e)) the anisotropy energy returns the magnetic moments to the easy c -axis of the crystal and the pinning site energy provides a restoring mechanism for the twin boundary, returning the sample to its original length and magnetization. This pinning site theory provides an explanation for the smaller magnitude of strain possible from this sample and for the reversibility of the strain when the magnetic field is cycled.

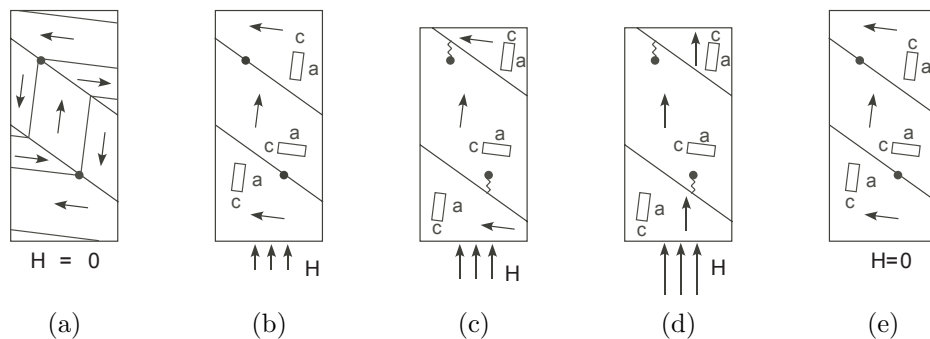


Figure 3. Strain mechanism for Ni-Mn-Ga driven by a collinear stress and field pair in the presence of pinning sites. (a) No field applied. (b) - (d) Sample contraction due to increasing field. (e) Return to original length when the field is removed.

3. MODEL

The strain produced by Ni-Mn-Ga driven by collinear magnetic fields and stresses is quantified in two steps. In the first, a thermodynamic approach is formulated which builds on a previous model for FSMA's proposed by Kiefer and Lagoudas¹² for conventional perpendicular magnetic fields and stresses. An additional term due to internal orthogonal stresses is included in the Gibbs energy function which quantifies the restoring force found in our experiments.⁷ The model quantifies the strain generated by single crystalline two-variant systems in which

the pinning density and magnetic field are homogeneous throughout. These conditions prove too limiting in real engineered materials. In the second step of model development, these limitations are addressed by considering a homogenization procedure first proposed by Smith¹³ whereby the pinning strength and local magnetic fields are stochastically distributed. This yields a formulation which characterizes the evolution of volume fractions in Ni-Mn-Ga alloys driven by collinear magnetic fields and stresses in the presence of internal restoring forces.

Free Energy Formulation

For simplicity, we assume that the structure comprises two variant orientations described by the two-dimensional representation shown in Figure 4. Variant 2 is that which is favored by an axially applied field in the y-direction and has a volume fraction of x . Variant 1 is the transverse variant with magnetization vectors oriented orthogonal to the applied field and a volume fraction of $(1 - x)$.

The material described in Figure 4 can be treated as a mixture of variants. Making the assumption that the system is isothermal and that the magnetic fields are large, the energy for this system is can be written as

$$G(\boldsymbol{\sigma}, \mathbf{H}, T) = (1 - x)G^{v1} + xG^{v2} + G^b \quad (1)$$

where G^{vi} is the energy of the i -th variant and is given by

$$G^{vi}(\boldsymbol{\sigma}, \mathbf{H}, T = \text{const}) = \psi^{vi} - \frac{1}{2\rho} \boldsymbol{\sigma} \cdot \mathbf{S}^{vi} \boldsymbol{\sigma} - \frac{\mu_0}{\rho} \mathbf{M}^{vi} \cdot \mathbf{H} \quad (2)$$

where for the i -th variant, ψ^{vi} is the Helmholtz energy, $\boldsymbol{\sigma}$ is the externally applied stress, \mathbf{S}^{vi} is the mechanical compliance, \mathbf{M}^{vi} is the magnetization, \mathbf{H} is the applied field, ρ is the density, and μ_0 is the permeability of free space.

The energy of the twin boundary stems from two sources. The first is the energy necessary to rotate a unit cell, which can be expressed as work done to overcome a force. The second is the energy of the pinning sites, which can be modeled as that of a mechanical spring. Thus the boundary energy term has the form

$$G^b = \begin{cases} c_1x + k_1x^2 & \dot{x} > 0 \\ c_2x + k_2x^2 & \dot{x} < 0 \end{cases} \quad (3)$$

where k is the effective spring constant of the pinning sites, c is the energy associated with cell reorientation and the two branches of the function occur because the behavior of the material is not the same when the field is increasing and variant 1 is growing as it is when the field is decreasing and variant 1 is shrinking.

Energy minimization, which is discussed in detail by Kiefer and Lagoudas,¹² and Faidley et al.^{7,14} are then used to derive a simplified kernel model for the volume fraction as axial magnetic fields and external loads are

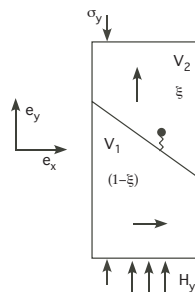


Figure 4. Two-dimensional variants: notation and orientation.

applied:

$$x = \begin{cases} \frac{1}{2\rho k_1}(\epsilon_s \sigma_y + \frac{1}{2}\Delta S_{yy} \sigma_y^2 + \mu_0 M_s H_y - \rho c_1 - Y^x) \\ x_s \\ \frac{1}{2\rho k_2}(\epsilon_s \sigma_y + \frac{1}{2}\Delta S_{yy} \sigma_y^2 + \mu_0 M_s H_y - \rho c_2 + Y^x) \end{cases} \quad (4)$$

for the respective cases $\{\dot{H} > 0 \text{ and } x < x_s\}$, $\{x > x_s\}$ and $\{\dot{H} < 0 \text{ and } x < x_s\}$. Where M_s is the saturation magnetization, ϵ_s is the saturation strain, ΔS_{yy} is the difference in the compliance of the two variants, and Y^x is the force necessary of the onset of variant reorientation. The strain is related to the volume fraction by

$$\epsilon = x\epsilon_{th}, \quad (5)$$

with ϵ_{th} the maximum theoretical strain which would occur if a single boundary swept through the entire material, thus producing a change in x from 0 to 1. Hence, for the case where the twin boundaries are restrained by pinning sites, x will be limited to a much smaller range. Parameters that need to be identified in this model include k_1 , k_2 , ϵ_s , ΔS_{yy} , M_s , c_1 , c_2 , and Y^x .

Stochastic Homogenization

Relation (4) provides a model for the strain generated by single crystal Ni-Mn-Ga with its twin boundaries partially restrained by pinning sites, exposed to collinear magnetic fields and external stresses. The limitations of the model and a sensitivity analysis relating model accuracy with parameter selection were discussed by Faidley et al.⁷ The most critical sources of error in this model include:

- (i) The sample is assumed to consist of only two variants with a single boundary. In reality, however, Ni-Mn-Ga has many twin variants though only two distinct orientations. This implies that a sample will have numerous twin boundaries and thus numerous pinning sites.
- (ii) The pinning sites are assumed to be homogeneously distributed throughout the material and every pinning site has the same energy. As discussed by Marioni,¹⁵ in a physical material the pinning energies vary over a large range which translates into a variation of the slopes k_1 and k_2 . The energy of each site depends on how it interacts with the surrounding microstructure. Furthermore, the strength of each site may depend on the direction of motion of the twin boundary, effectively providing a source of anisotropy.
- (iii) The field is assumed to be uniform throughout the sample. However, due to short-range interactions the magnetic field in Ni-Mn-Ga can be considered to behave locally in a fashion similar to the Weiss mean field.¹⁶ Thus, the magnitude of the field at a given point in the material is not equal to the applied field but rather, is given by an effective field which is dependent on the applied field and the magnetization, $H_e = H + H_i = H + \alpha M$. The mean field constant α varies from point to point in the material due to differences in the lattice structure.

Limiting factors (i)-(iii) are addressed in this paper by considering stochastic homogenization in the sense of Smith.¹³ The strain model for ferromagnetic shape memory materials presented in this article builds on the Smith model for hysteresis of ferroic materials but differs from it in the following aspects. (i) Kernel (4), which characterizes the martensitic volume fraction, was developed by considering the reorientation of twin variants in martensitic structures and therefore reflects energy functionals which are different from those found in polarization models. While certain commonality can be established between the proposed model and previous polarization models—e.g., in regard to double-well energy potentials—the difference between kernels is rooted in the physical differences between MFIS and magnetostriction, which were outlined by O’Handley.⁹ (ii) In this paper the stochastic homogenization is performed relative to the interaction field H_i and the pinning energy k_2 . This implies that suitable distributions to accommodate these effects can potentially be different than those employed for interaction and coercive fields by Smith.¹⁷ Notwithstanding, for the sake of simplicity, in this paper we attempt to exploit certain commonalities between the phenomenological behaviors observed in both models. Namely, for the interaction field we consider a normal distribution centered at $H_i = 0$, as in the Smith

model, and for the pinning sites we consider a log-normal distribution similar to that employed in¹⁷ for coercive fields.

The model thus has the form

$$[x(H, \sigma)](t) = \int_0^\infty \int_{-\infty}^\infty \nu_1(H_i) \nu_2(k_2) [\bar{x}(H + H_i; \sigma, k_2)](t) dH_i dk_2 \quad (6)$$

where ν_1 and ν_2 are appropriately chosen distributions and \bar{x} is given by expression (4). Since the Weiss interaction field is known to have both positive and negative values, one possible distribution is

$$\nu_1(H_i) = c_1 e^{-H_i^2/(2b^2)} \quad (7)$$

which is a normal distribution centered at $H_i = 0$. The pinning site energies were incorporated into the energy equations as effective mechanical springs. Thus, the values for k_2 will never be negative. To meet this criterion the distribution over k_2 is chosen to be log-normal and is given by

$$\nu_2(k_2) = c_2 e^{-(\ln(k_2/\bar{k}_2)/2c)^2} \quad (8)$$

4. EXPERIMENTS

A single crystal alloy with composition $\text{Ni}_{50}\text{Mn}_{28.7}\text{Ga}_{21.3}$ was tested for strain response under a [001] sinusoidal magnetic field with an amplitude of 700 kA/m and collinear compressive stresses of 0.0125 MPa, 0.13 MPa, 0.27 MPa, and 0.41 MPa. The single crystal ingot, prepared by the Bridgman method at Ames Laboratory, was oriented along the [001] direction and a 0.248 in (0.630 cm) diameter, 0.883 in (2.243 cm) long rod was cut from the ingot using electrical discharge machining (EDM). The experiments were conducted with a collinear magnetic field-stress pair in the solenoid transducer shown in Figure 5, which consists of a water-cooled solenoid, pickup coil, and magnetic steel components integrated to form a closed magnetic circuit. The solenoid consists of 1350 turns of AWG 15 magnet wire and has a field rating of 167 Oe/A. Interspersed within the solenoid lies a 0.25 in-diameter copper coil which provides temperature control within ± 1 °F by means of water flow at a rate of up to 6.35 L/min. The solenoid is driven by two Techron 7790 4 kW amplifiers arranged in series with an overall voltage gain of 60 and a maximum output current of 56 A at the nominal solenoid resistance of 3.7 Ω . The magnetic induction is measured with a pickup coil made from AWG 33 insulated copper wire wound in two layers around an aluminum spool. The strain is measured by means of a Lucas Shaevitz MHR-025 linear variable differential transducer (LVDT) attached to the pushrod. Several Omega thermocouples are used to monitor the system temperature through a 10-channel Omega signal conditioner. The system is controlled by a DataPhysics data acquisition system interfaced through a PC.

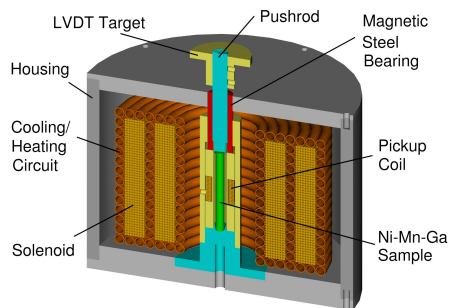


Figure 5. Cross-section of the solenoid transducer employed in this study.

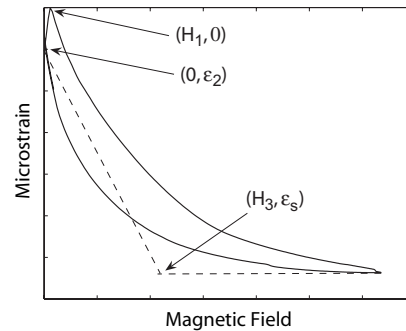


Figure 6. Data points used for identification of model parameters.

5. MODEL IMPLEMENTATION

The homogenized strain relation (6) was approximated through a composite four-point Gauss-Legendre quadrature routine over twenty six intervals in both H_i and k_2 . Parameters ΔS_{yy} , M_s and Y^ξ were obtained from published data.¹² As shown in Figure 6, three data points provide the following information: (i) field H_1 at the strain turn around point, (ii) strain ϵ_2 at the cross over point, (iii) field H_3 at the onset of saturation, and (iv) saturation strain for each loading case, $\epsilon_s(\sigma_p)$. Values and expressions for the various model parameters are given in Table 1. Coefficients c_1 and c_2 in equation (4) were determined from experimental data following techniques used by Kiefer and Lagoudas.¹² Distribution parameters \bar{k}_2 , b , and c and kernel parameter n were determined through constrained optimization to minimize the total difference between the time trace strain data and the output of the model for each of the loading conditions.

Table 1. Values for model coefficients.

Change in mechanical compliance between variants	$\Delta S_{yy} = 0$
Saturation magnetization	$M_s = 622 \text{ kA/m}$
Onset of variant reorientation	$Y^x = 0.2 \times 10^6 \text{ N/m}^2$
Theoretical maximum strain	$\epsilon_{th} = -60,000 \times 10^{-6}$
Density	$\rho = 1$
Cell reorientation energy, variant 1	$c_1 = \epsilon_s(\sigma_p)\sigma_p + \frac{1}{2}\Delta S_{yy}\sigma_p^2 + \mu_0 M_s H_1 - Y^x \text{ J/m}^3$
Cell reorientation energy, variant 2	$c_2 = \epsilon_s(\sigma_p)\sigma_p + \frac{1}{2}\Delta S_{yy}\sigma_p^2 + Y^x - 2k_2 \frac{\epsilon_2(\sigma_p)}{\epsilon_{th}} \text{ J/m}^3$
First turnaround point	$H_1 = 10,750 \text{ A/m}$
Coercive field distribution	$H_{i,max} = 350 \text{ kA/m}, H_{i,min} = 0$
Pinning energy distribution	$k_{2,max} = 2.7 \times 10^6, k_{2,min} = 2 \times 10^5, \bar{k}_2 = 1.23 \times 10^6$
Standard deviations	$b = c = 1 \times 10^6$

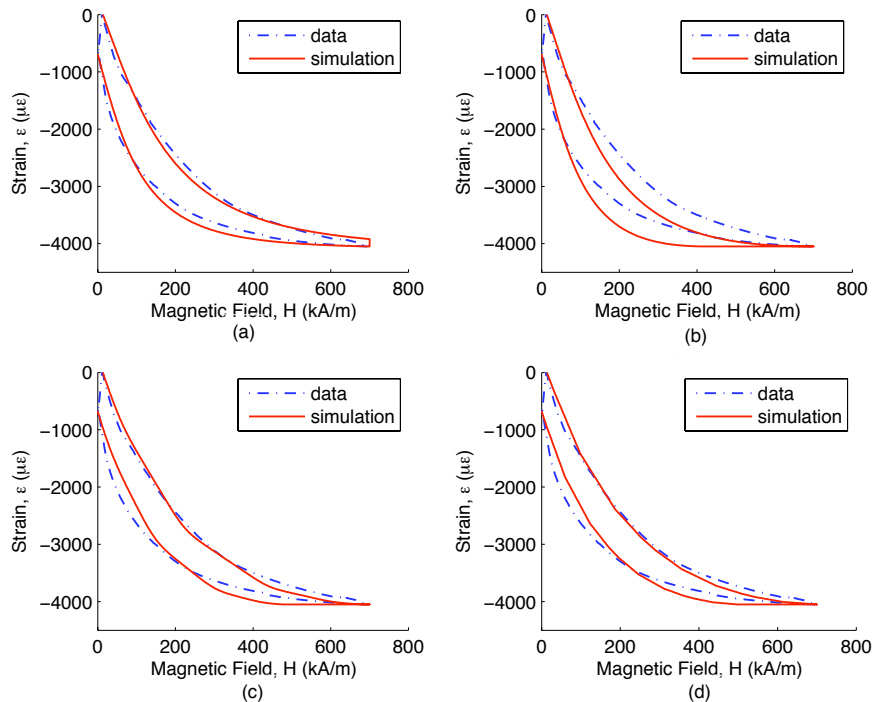


Figure 7. Comparison of model results and experimental data for the $\sigma = -0.0125 \text{ MPa}$ loading condition using various implementation methods: (a) using full distribution, (b) using method (i), (c) using method (ii), and (d) using method (iii).

As an example, a calculated strain versus magnetic field curve is compared to data for the $\sigma = -0.0125$ MPa loading condition in Figure 7(a). The calculated curve shows a non-physical blocky tip due to the inclusion of kernels which fall into non-physical ranges of k_1 and H_i . Figure 8 shows an example of a standard kernel given by relation (4). In the range of parameters where a large k_1 is combined with a large H_i , non-physical kernels with a discontinuity at the maximum field will result. Three methods are considered for addressing this anomalous behavior:

1. Discard the kernels that yield non-physical results among the set of kernels found through constrained optimization and the full distributions (7)-(8), and calculate relation (6) based on the reduced set.
2. Truncate the distributions (7)-(8) such that the range of pinning energies and interaction fields that yield non-physical behaviors are discarded, identify new parameters through constrained optimization, and calculate relation (6) based on the truncated distributions.
3. Impose the restriction directly on the bounds employed in the constrained optimization algorithms, such that all the resulting kernels are forced to yield physical results.

The results obtained with these three methods for the $\sigma = -0.0125$ MPa loading condition are shown in Figure 7(b)-(d), while the associated model errors are quantified in Table 2. All three methods yield results without the non-physical discontinuity at maximum field. As expected, the error is greatest for the first method where the non-physical kernels are ignored without recalculating the parameters. The lowest error is achieved using method 3, in which the constrained optimization routine includes the inequality

$$\frac{1}{2\rho k_{1,max}} \left(\epsilon_s \sigma_y + \frac{1}{2} \Delta S_{yy} \sigma_y^2 + \mu_0 M_s (H_{max} - H_{i,max}) - \rho c_1 - Y^x \right) \geq p \frac{\epsilon_s}{\epsilon_{th}} \quad (9)$$

which is derived from expression (4) and places limits on the distribution coefficients and therefore the shape of the distributions. Parameter p is introduced to control the percentage of the kernels that are allowed to be non-physical and thus define both the range of allowable distribution shapes and how much of each distribution is truncated. The maximum values for k_1 and H_i are found from expressions (7) and (8),

$$H_{i,max} = \sqrt{-2(\bar{b})^2 \ln(.01)} \quad (10)$$

$$k_{1,max} = n \bar{k}_2 e^{2c\sqrt{-\ln(.01)}}. \quad (11)$$

Testing shows that $p = 0.1$ achieves a suitable balance between allowable shape of the distributions and the truncation of those distributions which best minimizes the error. An example of the truncated distributions that result from this kernel reduction scheme are shown in Figure 9. Method 3 with $p = 0.1$ is used in the following section to study the error for all four loading conditions.

6. RESULTS

Constrained optimization was used to determine the parameters for each of the four loading cases based on the minimization of the total sum of the error between the modeled and measured time traces of the strain. These parameters, shown in Table 3, were found to be within 10% of those necessary to minimize the mean error in

Table 2. Error associated with each of the methods used to eliminate the discontinuity at maximum field.

	Original	Method (i)	Method (ii)	Method (iii) w/ p = 0.1
Σe	42,382	130,000	71,818	69,960
$\langle e \rangle$	52.324	160.64	88.665	86.371
$\langle e \rangle / \epsilon_s (\%)$	1.3	3.9	2.2	2.1
max(e)	334.15	447.56	361.75	379.94

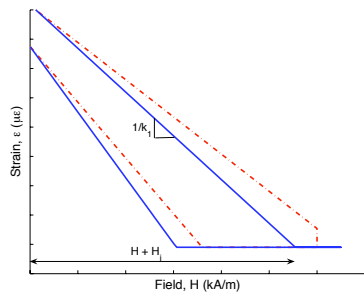


Figure 8. Hysteresis kernels produced by relation (4) showing both physical and non-physical behaviors.

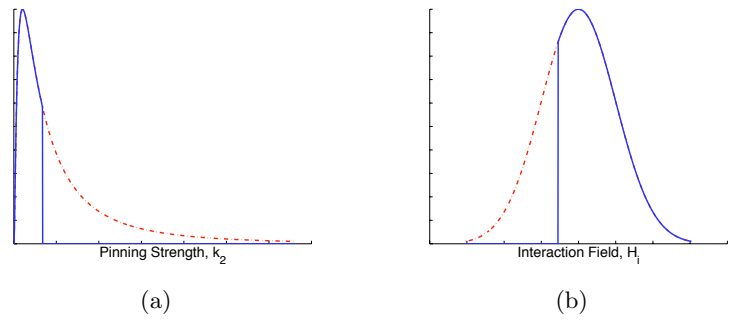


Figure 9. Truncated distributions for (a) pinning site strength k_2 and (b) interaction field H_i .

Table 3. Constrained optimization results for parameters under various loads.

	$\sigma = -0.0125$ MPa	$\sigma = -0.13$ MPa	$\sigma = -0.27$ MPa	$\sigma = -0.41$ MPa	Overall Optimal
n	1.165	1.1417	1.0894	1.0287	1.1207
\bar{k}	1.0306×10^6	0.70091×10^6	0.87182×10^6	1.3363×10^6	0.75325×10^6
c	0.80761	1	1	0.99856	0.99901
\bar{b}	0.010001×10^4	0.012166×10^4	0.01×10^4	0.01×10^4	0.010304×10^4

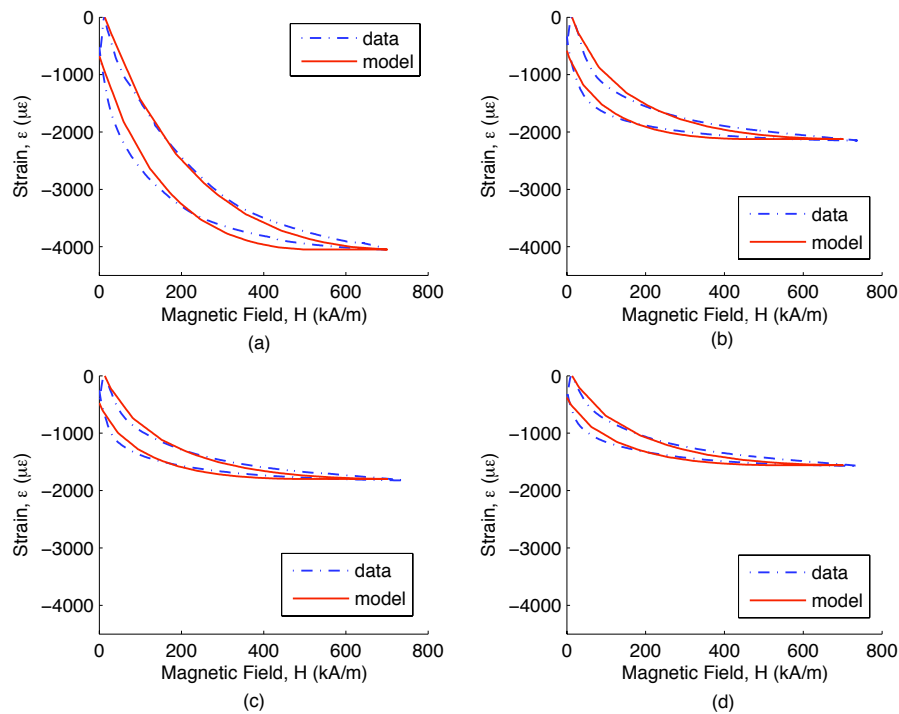


Figure 10. Constrained optimization fits to data for various loads: (a) $\sigma_y = -0.0125$ MPa, (b) $\sigma_y = -0.13$ MPa, (c) $\sigma_y = -0.27$ MPa, (d) $\sigma_y = -0.41$ MPa.

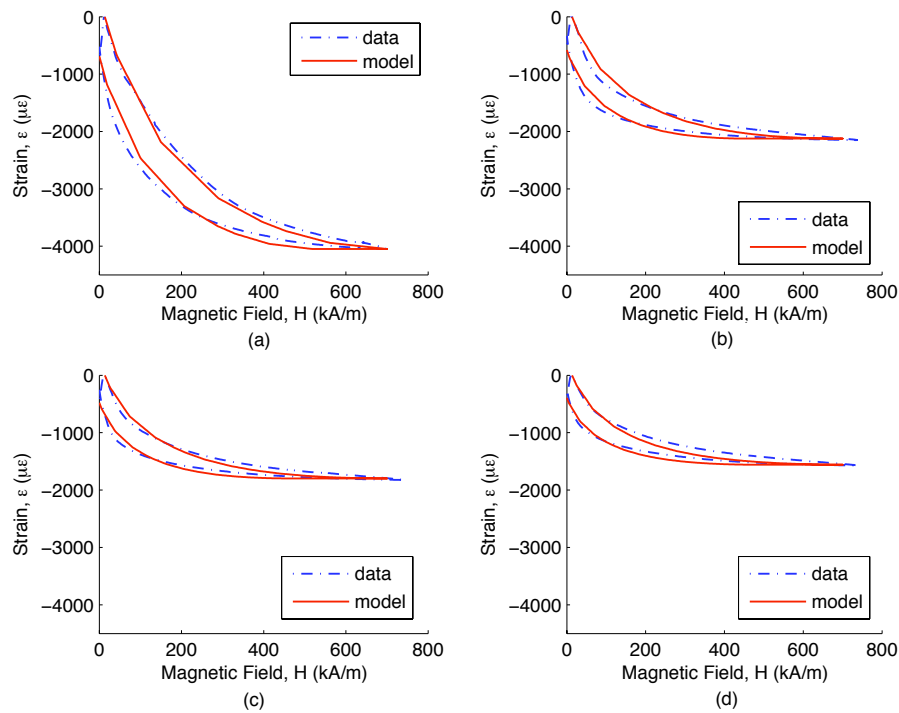


Figure 11. Overall optimized simulation of strain compared to data for various loads: (a) $\sigma_y = -0.0125$ MPa, (b) $\sigma_y = -0.13$ MPa, (c) $\sigma_y = -0.27$ MPa, (d) $\sigma_y = -0.41$ MPa.

all but two cases. A comparison of the data and the model for each of these loading cases is shown in Figure 10 where it is observed that the simulation closely predicts the data in all cases.

The last column in Table 3 represents the set of parameters found by minimization of the sum of the error across all four loading cases. A comparison between the data and the model results generated with these parameters is shown in Figure 11. Even though these simulations are generated from parameters optimized for overall reduction of error, the predictions are remarkably similar to those obtained using parameters optimized for individual cases in Figure 10. This is an indication that there are multiple minima in the four parameter optimization problem and hence various sets of parameters may produce similarly low values of the error. Figure 11 shows that the optimized parameters allow good correlation with data for the lower three load conditions but the model loses accuracy at the higher load case. This is because the error increase is much steeper for overestimation than for underestimation.

A quantitative look at the error calculations for the constrained optimization for various loading conditions is provided in Table 4. The error measurements calculated include the sum of the error which was the basis for the constrained optimization, the mean of the error, the percent error of the mean with respect to the maximum strain, and the maximum error. The error was calculated as the absolute value of the difference between the data and model at each point. The diagonal of Table 4 indicates the smallest error for all loading values and represents the cases in which the parameters were optimized for the same loading case as that being simulated, which corresponds to the plots shown in Figure 10. The off-diagonal values indicate the error for the cases in which the model parameters were optimized for a load other than the one used in the model. The errors are much larger below the diagonal where parameters for a higher load are used to simulate a lower load than above the diagonal where the reverse is true.

The rightmost column of Table 4 presents the sum of the errors for all four loading conditions for each set of parameters. For all four individually optimized cases the sums of the errors show only an 8% deviation. The bottom row of the table shows the model error when the set of parameters that minimizes the overall error is

Table 4. Error comparison for parameters determined for various loading conditions.

Parameter Set σ_p	Loading Conditions, σ_y				Total
	-0.0125 MPa	-0.13 MPa	-0.27 MPa	-0.41 MPa	
-0.0125 MPa					
Σe	69,960	40,393	35,767	37,644	183,764
$\langle e \rangle$	86.371	49.868	44.157	46.474	
$\langle e \rangle / \epsilon_s (\%)$	2.1315	2.3049	2.4111	2.9475	
max(e)	379.94	320.68	222.52	164.08	
-0.13 MPa					
Σe	81,910	35,180	31,667	36,508	185,265
$\langle e \rangle$	101.12	43.432	39.095	45.072	
$\langle e \rangle / \epsilon_s (\%)$	2.4957	2.0035	2.1312	2.8564	
max(e)	272.85	319.42	233.88	175.12	
-0.27 MPa					
Σe	81,136	39,571	29,586	31,938	182,231
$\langle e \rangle$	101.17	48.853	36.526	39.430	
$\langle e \rangle / \epsilon_s (\%)$	2.4724	2.2569	1.9908	2.4976	
max(e)	344.17	312.7	225.73	225.73	
-0.41 MPa					
Σe	83,168	51,065	37,442	26,615	198,290
$\langle e \rangle$	102.68	63.043	46.224	32.858	
$\langle e \rangle / \epsilon_s (\%)$	2.5351	2.9196	2.5252	2.0802	
max(e)	455.00	406.91	251.42	189.65	
Optimized					
Σe	64,106	37,297	30,965	31,454	163,822
$\langle e \rangle$	79.143	46.045	38.228	38.832	
$\langle e \rangle / \epsilon_s (\%)$	1.9516	2.1255	2.0838	2.4590	
max(e)	324.36	317.76	231.11	171.67	

used. This total is 12.5% lower than the average sum for the individually optimized cases. In addition, the sum of the error for each loading condition using these overall optimized parameters is within 20% of the minimum sum of the error found for the individually optimized parameters. The maximum is 18% for the $\sigma_y = -0.41$ MPa loading condition which corresponds to the observation made earlier with regard to the decrease in accuracy of the simulations shown in Figure 11 for the higher loading condition. The small differences between the simulations using the four-case optimization parameters and those using the individually optimized parameters highlights the ability of the homogenized model to quantify—from a single set of parameters—the strain produced by Ni-Mn-Ga for various loading conditions. With mean errors of under 3%, this modeling technique shows promise for design and control applications involving solenoid-based Ni-Mn-Ga actuators.

7. CONCLUDING REMARKS

This paper presents a model for the strain produced by Ni-Mn-Ga alloys subjected to magnetic fields and stresses aligned along the [001] axis of the parent austenitic phase. This is an unusual configuration which was implemented in this paper through a solenoid transducer featuring a closed magnetic circuit. Due to the reduced demagnetization effects and reduced eddy current losses of this architecture relative to electromagnet designs, it can potentially lead to faster and more energy efficient Ni-Mn-Ga actuators and sensors. The paper provides a thermodynamic framework which quantifies reversible and irreversible processes associated with the rotation of twin variants. The switching between two variant orientations in the presence of magnetic fields (Zeeman energy) and pinning sites (pinning energy) is formulated through a Gibbs energy functional which is accurate for defect-free single crystal materials. Assumptions at this stage include that the alloy consists of only two variants with pinning sites and magnetic fields homogeneously distributed throughout the material. The presence of local interaction fields, and inhomogeneous pinning sites in real Ni-Mn-Ga alloys is addressed through a stochastic homogenization procedure. Attributes of the model are illustrated through comparison of

model results with experimental measurements collected from a $\text{Ni}_{50}\text{Mn}_{28.7}\text{Ga}_{21.3}$ sample. Use of a constrained optimization technique indicates the ability of the model to accurately simulate the strain output to within a mean error of 3% for compressive loading between 0–0.41 MPa.

ACKNOWLEDGMENTS

The authors thank Ralph Smith and Björn Kiefer for useful discussions, and Thomas Lograsso for supplying the Ni-Mn-Ga material. The work of L.E.F. is supported by a graduate fellowship from the Ohio Space Grant Consortium. The work of M.J.D. is supported in part by NSF grant #CMS-0409512.

REFERENCES

1. S. Murray, M. Marioni, P. Tello, S. Allen, and R. O’Handley, “Giant magnetic-field-induced strain in Ni-Mn-Ga crystals: experimental results and modeling,” *Journal of Magnetism and Magnetic Materials*, **226-230**, pp. 945–947, May 2001.
2. A. Likhachev, A. Sozinov, and K. Ullakko, “Influence of external stress on the reversibility of magnetic-field-controlled shape memory effect in Ni-Mn-Ga,” *Proceedings of SPIE Smart Structures and Materials Conf.*, **4333**, pp. 197–206, 2001.
3. A. Sozinov, A. Likhachev, N. Lanska, and K. Ullakko, “Giant magnetic-field-induced strain in NiMnGa seven-layered martensitic phase,” *Applied Physics Letters*, **80**, pp. 1746–1748, March 2002.
4. L. E. Faidley, M. J. Dapino, G. N. Washington, and T. A. Lograsso, “Dynamic response in the low-kHz range and Delta-E effect in ferromagnetic shape memory Ni-Mn-Ga,” *Proceedings of IMECE 2003* (43198), 2003.
5. R. Tickle, *Ferromagnetic Shape Memory Materials*. PhD thesis, Texas A&M, 2000.
6. A. Malla, M. Dapino, T. Lograsso, and D. Schlager, “Large magnetically-induced strains in $\text{Ni}_{50}\text{Mn}_{28.7}\text{Ga}_{21.3}$ driven with collinear field and stress,” *Journal of Applied Physics*, (In review).
7. L. Faidley, M. Dapino, G. Washington, and T. Lograsso, “Reversible strain in Ni-Mn-Ga with collinear field and stress,” *Proc. SPIE Smart Structures and Materials* (5761), pp. 501–512, 2005.
8. M. L. Richard, *Systematic analysis of the crystal structure, chemical ordering, and microstructure of Ni-Mn-Ga ferromagnetic shape memory alloys*. PhD thesis, Massachusetts Institute of Technology, Sept. 2005.
9. R. C. O’Handley, S. Murray, M. A. Marioni, H. Nembach, and S. Allen, “Phenomenology of giant magnetic-field induced strain in ferromagnetic shape-memory materials,” *J. Appl. Phys.*, **87**, pp. 4712–4717, May 2000.
10. R. Tickle and R. James, “Magnetic and magnetomechanical properties of Ni_2MnGa ,” *Journal of Magnetism and Magnetic Materials (Netherlands)*, **195**, pp. 627–638, June 1999.
11. A. Likhachev and K. Ullakko, “Magnetic-field-controlled twin boundaries motion and giant magneto-mechanical effects in Ni-Mn-Ga shape memory alloy,” *Physics Letters A*, , pp. 142–151, October 2000.
12. B. Kiefer and D. C. Lagoudas, “Phenomenological modeling of ferromagnetic shape memory alloys,” *Proceedings of SPIE Smart Structures and Materials Conf.*, **5387**, pp. 164–176, July 2004.
13. R. C. Smith, *Smart Material Systems: Model Development*, Society for Industrial & Applied Mathematics, Philadelphia, PA, 2005.
14. L. Faidley, *Characterization and Modelling of Ferromagnetic Shape Memory Ni-Mn-Ga in a Collinear Stress and Field Configuration*. PhD thesis, The Ohio State University, 2005.
15. M. A. Marioni, S. M. Allen, and R. C. O’Handley, “Nonuniform twin-boundary motion in Ni-Mn-Ga single crystals,” *Applied Physics Letters*, **84**, pp. 4071 – 4073, May 2004.
16. D. Jiles, *Magnetism and Magnetic Materials*, Chapman & Hall, 1995.
17. R. Smith, M. Dapino, T. Braun, and A. Mortensen, “A homogenized energy framework for ferromagnetic hysteresis,” *IEEE Transactions on Magnetics*, (in review).